Three-dimensional definition of two prominent deep brain stimulation targets based on a multimodal high-definition MNI template

Siobhan Ewert[1] and Andreas Horn[1,2]

1) Charité – University Medicine, Neurology Department, Movement Disorders Section, KFO 247 (Berlin, Germany)

2) Harvard Medical School, Beth Israel Deaconess Medical Center, Neurology Department, Berenson-Allen Center for Noninvasive Brain Stimulation, Laboratory for Brain Network Imaging and Modulation (Boston, MA, USA)

Manuscript metrics

Title character count: 111

Number of references: 64

Number of tables: 1

Number of figures: 7

Word count text: 6,401

Corresponding Author

Dr. Andreas Horn

Department for Neurology, Movement Disorders Unit Charité – University Medicine (CVK), Augustenburger Platz 1, 13353 Berlin, Germany;

E-mail: andreas.horn@charite.de

Phone : +49 (0)30 450 660 279

Siobhan Ewert: siobhan.ewert@charite.de

Keywords: deep brain stimulation, dystonia, parkinson's disease, MNI, subthalamic nucleus, globus pallidus, atlas.

Highlights:

- High definition atlas of DBS targets exactly matching MNI 152 NLin 2009 space
- Multimodal subcortical segmentation algorithm applied to MNI template
- Profound literature overview about available subcortical atlases and their use cases and potential limitations

Abstract

Three-dimensional atlases of subcortical brain structures are valuable tools to reference anatomy in neuroscience and neurology. In the special case of deep brain stimulation (DBS), the two most prominent targets are the subthalamic nucleus (STN) and the internal part of the pallidum (GPi). With the help of atlases that define their position and shape within a well-defined stereotactic space, their spatial relationship to implanted deep brain stimulation (DBS) electrodes may be analyzed on a single-subject level and in group studies. One standard approach to define such atlases is to manually segment structures on MR data of large cohorts and coregister them to a standard anatomy template. Other approaches include using histological stacks that are again co-registered to the template. However, most of the atlases derived in this fashion show a substantial descripancy to the anatomy that is defined by the template itself. Here, an algorithm that automatically segments the template itself by simultaneously using its T1, T2, proton density and T2 relaxometry modalities is introduced. Based on a low number of manually placed point fiducials within each structure, this three-level algorithm was able to robustly segment subcortical anatomical structures. The first level consisted of a multimodal region-growing algorithm that intended to increase the number of sample points for robustness reasons. The second level computed Mahalanobis distances from each voxel in the brain to the multimodal intensity distribution of first level points set and thus assigned target structure similarity values to each voxel. Finally, the third level assigned each super-threshold voxel to one of the subcortical structures in a winner-takes-all fashion based on second level probability maps. The algorithm was able to segment the STN, the pallidum and the red nucleus directly on the MNI

template. The algorithm was not able to automatically segment the internal and external parts of the pallidum. However, given the practical importance of the GPi, a second version of the atlas was defined in high resolution by manual segmentation. To maintain a maximally possible observer-independence, this process was largely informed by automatically generated probability maps described above. We argue that the resulting atlas is a valuable tool to define DBS target structures within standard anatomical space. Furthermore, the atlas may additionally be used as an anchor-point to co-register more detailed (e.g. histological) atlases into standard space. Both the automated and manual versions of the atlas will be made publicly available under an open license.

Introduction

Three-dimensional subcortical atlases are valuable tools to reference anatomy in the brain. In the field of deep brain stimulation (DBS), atlases of certain target structures may be used to study the relationship of electrode placement to the structure in subcortical space (Merkl et al. 2014; Merkl et al. 2015; Butson et al. 2007; Eisenstein et al. 2014; Horn & Kühn 2015; Neumann, Jha, et al. 2015; Neumann, Staub, et al. 2015; Barow et al. 2014; Welter et al. 2014). Most of the atlases available have been defined by the use of histology or various forms of magnetic resonance imaging (MRI). For instance, the atlases by Yelnik et al. (Yelnik et al. 2007) and Chakravarty et al. (Chakravarty et al. 2006) were defined by using histological slices and staining of a single brain. Mai et al. defined a histological atlas based on three brains (Mai et al. 2007) and Morel et al. used maps derived from histological stacks of six brains (Morel 2013). The latter atlas was digitized (Krauth et al. 2010) and warped into a standardized stereotactic

(*MNI152*) space (Jakab et al. 2012) in further studies. In the case of the Chakravarty study, the atlas was co-registered to an MRI template after matching the intensities of histological sub-structures to the ones of the MRI and applying a linear transformation to the dataset. In this fashion, the atlas was transformed into a common space (*colin27*) to allow for conclusions in standardized brain anatomy. The BGHAT atlas, in contrast, was defined by manual delineation of subcortical structures on a single MRI image (Prodoehl et al. 2008). Similarly, the CFA subcortical shape atlas was manually delineated on MRI, but used acquisitions of 41 subjects (Qiu et al. 2010). The ATAG atlas used multimodal high field MRI to estimate structures of the basal ganglia on a series of images (Keuken et al. 2014) and even included three probabilistic maps of the subthalamic nucleus (STN) based on cohorts with varying age (Keuken et al. 2013). In a study by Lenglet et al., a comprehensive atlas of basal ganglia structures and their white-matter interconnections was established using structural and diffusion-weighted MRI (Lenglet et al. 2012). Finally, the MIDA model (Iacono et al. 2015) focused on a detailed whole-head segmentation that included structures like blood vessels, muscles and bones but also covered subcortical structures of the brain including the STN.

Despite the high precision of anatomical labels in histological atlases and the probabilistic nature of atlases derived from larger cohorts of subjects, a problem may be entailed in the use of such atlases to label a subject's anatomy: In theory, in any standardized stereotactic space, only one «truth» exists – the one of the template (but see discussion). Any standardized stereotactic space *is defined* solely by its anatomical template(s). In other words, these templates define which anatomical structure is located at any given Cartesian coordinate. The STN is a

good example to further illustrate the issue. The nucleus is well visible as a hypointense lentiform structure on T2-weighted versions of, for instance, the ICBM 152 2009b nonlinear asymmetric template (**Figure 2**, upper left panel). If used in a nonlinear normalization process, this means that a good algorithm will try to warp the nucleus from the single subject anatomy onto this hypointense lentiform structure defined by the template. In theory, a perfect algorithm would even obtain a solution that renders a patient's STN equally lentiform, equally sized and placed at the exact same spatial position as the one in the template. The better the algorithm, the better it will achieve this goal (Klein et al. 2009; but see discussion). Strictly speaking, in the field of DBS imaging, since the STN of a patient is being deformed in such a process, the DBS electrodes of the same patient might thus be warped to appear smaller or larger, they might even form a bend in some cases. In MNI space, however, the STN itself should always appear at the same position and have the same shape and size (the one of the template; **Figure 1**). In other words, the MNI space itself is a Euclidean space as is the native space of any patient's brain anatomy. If, however, a single patient's anatomical space is being warped into MNI space, the former will become curved and distorted.

Contrastingly, STN parcellations of available atlases do not necessarily match the size, position and shape of the hypodense area that marks the STN inside the MNI templates (**Figure 2**). Depending on which atlas is being used to define the STN in standard space, substantially different results will be obtained. Various reasons may explain this disagreement. First, some atlases have been registered to different brain templates than the one adopted to define standard anatomy by the International Consortium for Brain Imaging (ICBM 152 2009 nonlinear

template series; Fonov et al. 2011). Various spatial standard templates exist, most of which represent a function of the historical development of nonlinear warping techniques (Ashburner 2012; Fonov et al. 2011; Fonov et al. 2009; Allen et al. 2002) or of differing underlying populations (Liang et al. 2015). Even two MNI template series labeled as *MNI152* exist. The first one, the successor of the MNI305 (Collins 1994), was adopted as the standard template for brain anatomy by popular fMRI processing suites such as SPM (http://www.fil.ion.ucl.ac.uk/spm/; since version SPM99) and FSL (http://fsl.fmrib.ox.ac.uk/fsl/fslwiki/). Here, MRI acquisitons of 152 subjects were *linearly* co-registered to the *MNI305* space (see Brett et al. 2002 for an overview). In the second version introduced in 2009, the acquisitions were instead *nonlinearly* co-registered (Fonov et al. 2011b). Notably, within this series, the 2009b template is the only one that exhibits a resolution as high as 0.5 mm. As a parallel offspring, the MNI generated a single-subject template in similar space by scanning a subject 27 times. This template is referred to as the *colin27* space and is again used to define single subject anatomy in SPM and FSL. Lastly, templates that are based on populations of different ethnicity (e.g. see Liang et al. 2015) or ones that focus on parts of the brain such as the cerebellum (Diedrichsen et al. 2011) exist. All of these many standard templates roughly define the space that is often simply referred to as the *MNI space*. In the field of fMRI imaging, where spatial resolution of most studies ranges within the magnitude of 2-3 mm, slight inaccuracies introduced by a mixed use of templates may not lead to significant errors. In DBS imaging, however, millimeters do matter (Frankemolle et al. 2010; Yelnik et al. 2003; Horn & Kühn 2015b; Pollo et al. 2004). Further reasons that may explain slight disagreements between available atlases and the ICBM 2009b nonlinear template anatomy may be that co-registration algorithms led to inaccuracies of structure

placement or that the number of volumes acquired for atlas generation differed from the ones acquired for template generation. For instance, one version of the ATAG atlas is based on 30 subjects with a mean age of 24.2 (Keuken et al. 2014) whereas subjects of the MNI 152 database range from birth to adulthood (Fonov et al. 2011b). Where the MNI 152 2009 nonlinear templates were constructed using nonlinear transforms estimated by MINC Tool Kit software (http://www.bic.mni.mcgill.ca/ServicesSoftware/ServicesSoftwareMincToolKit), the ATAG atlas was constructed using linear AC/PC transforms (which are comparable to Talairach transforms (Brett et al. 2002)). Ultimately, a different spatial definition is prone to result given the large differences in data used and methods applied and it is important to mention that this was exactly the goal of the ATAG experiment: To uncover variability of basal ganglia anatomy (and not to segment basal ganglia from the ICBM template). Lastly, some reasons for incongruence between atlas and template structures should be attributed differently and again, the STN is a good example. Given an inhomogeneous distribution of iron-density in the nucleus, its medioventral portion shows up more hypointense than its dorsolateral parts (Dormont et al. 2004; de Hollander et al. 2014; Schäfer et al. 2011). This may lead to a smaller representation of the STN on standard MRI and greatly justifies the use of histological atlases or imaging techniques that are more sensitive to iron, such as quantitative subceptibility mapping (Wang & Liu 2015). Nevertheless, a meticulous co-registration between atlas sources and the standard template as well as the use of the same template in atlas generation and subsequent application procedures is important.

Here, we chose a rather unconventional strategy to outline anatomical labels in standard space. Namely, a multimodal subcortical segmentation algorithm was developed that segmented anatomical structures from the template itself. The algorithm worked on T1- and T2-weighted as well as proton density (PD) and T2 relaxometry (T2rlx) versions of the ICBM 2009 nonlinear template simultaneously and was able to outline subcortical structures in an automated, observer-independent fashion.

It was not the goal of this study to create a subcortical atlas that is superior in anatomical detail to the ones that have been published before. On the contrary, the ICBM template is not suited for e.g. estimating atlases in a probabilistic fashion and it does lack the anatomical precision of histological stains. Rather, the goal was to define an atlas that will maximally agree with the spatial extent and position of the structures defined on the template. The results may serve to identify spatial relationships of DBS electrodes and their most common target structures, the STN and pallidum. The structures outlined may additionally serve as reference points for registrations of more detailed atlases in the future.

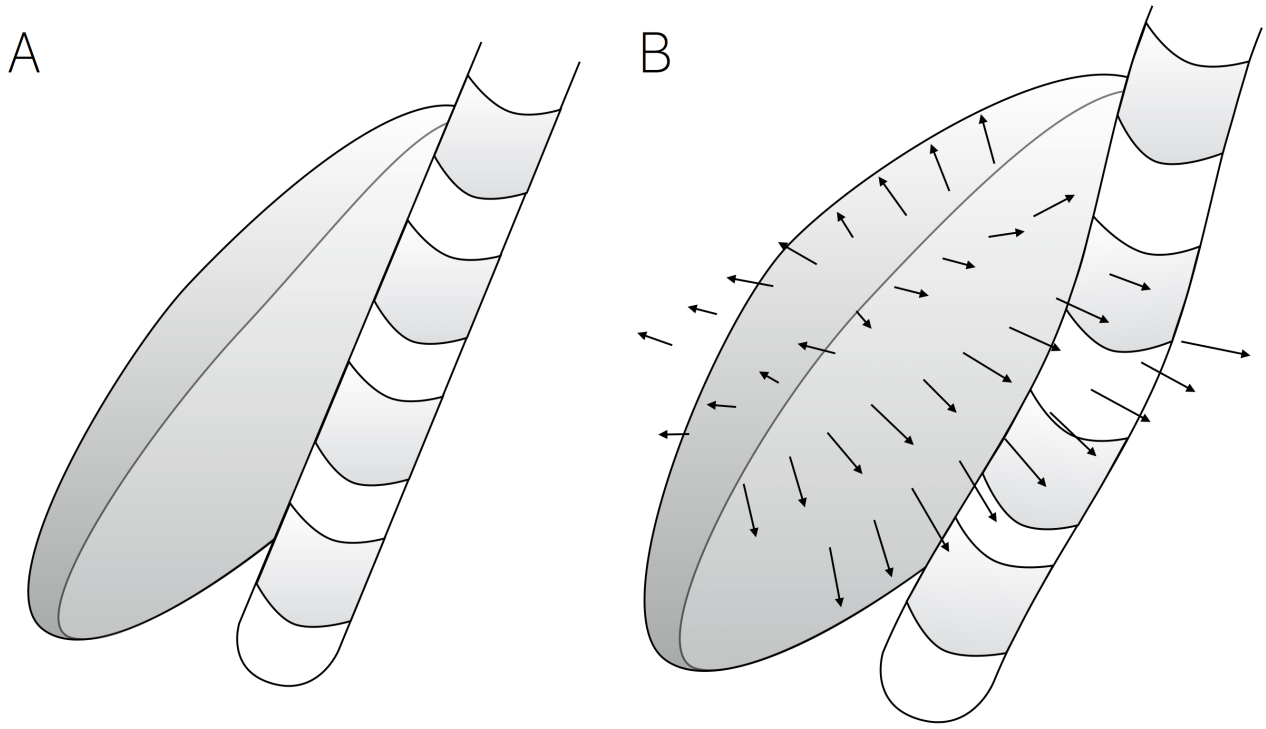

Figure 1: Relationship of a DBS electrode and the STN of a hypothetical patient in native single subject space (A) and standardized stereotactic (MNI) space (B). In standard space, the STN is defined once and for all based on the particular template. Arrows exemplarily illustrate the deformation field estimated to warp the (smaller) STN of the patient into the (larger) STN defined by the template. Note that this deformation leads to a bend in the DBS electrode and may also break up the distribution of electrode contacts (placed equidistantly on a straight line in A and on a curve with heterogeneous distances in B).

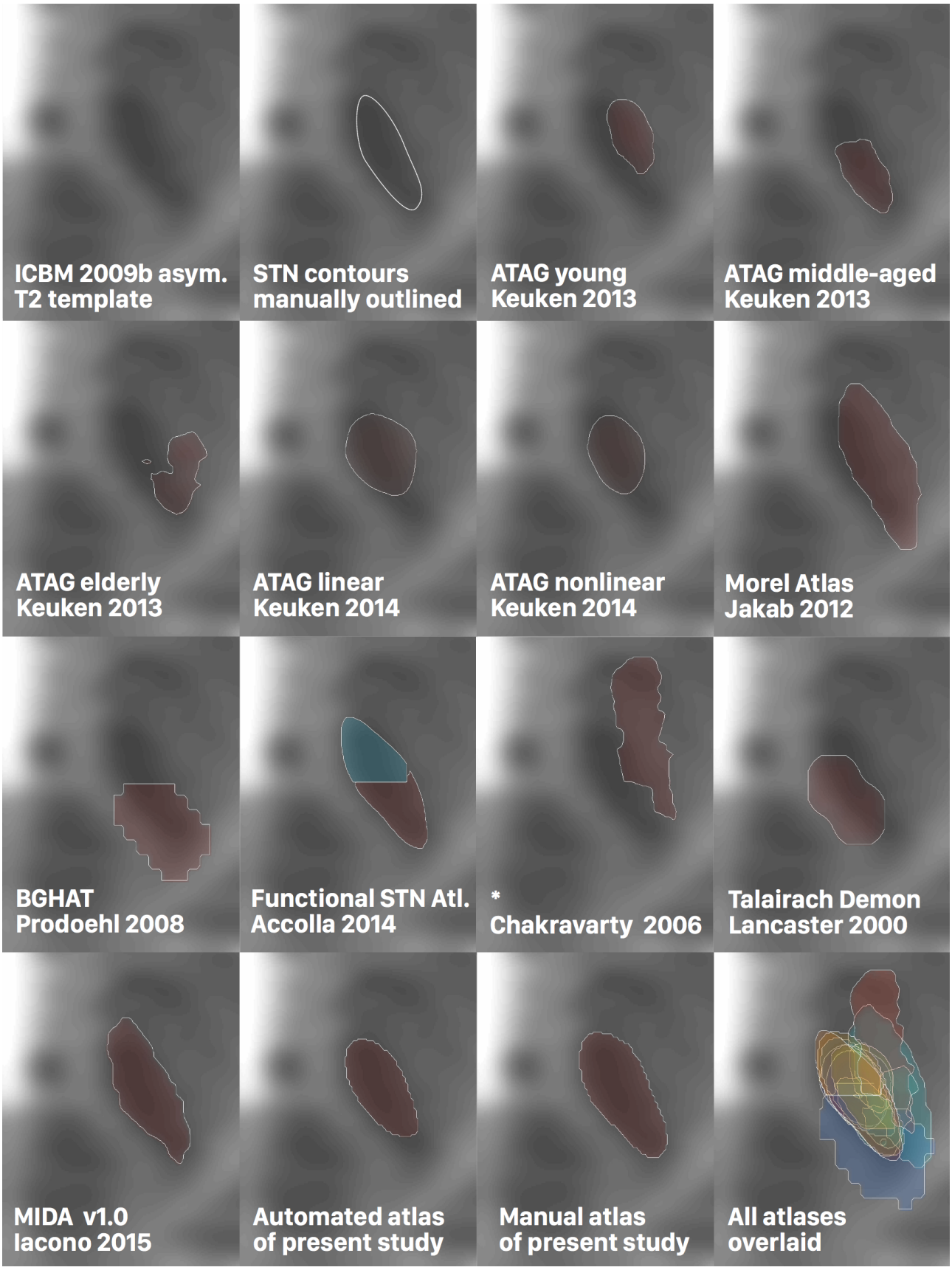

Figure 2: Which one is «correct»? Comparison of the ICBM 152 2009b template and various atlases of the STN available in standard space. First (upper left)

panel: The hypointense lentiform region of the STN defined by the template may clearly be identified (contours outlined in second panel). Subsequent panels show definitions of the STN based on various atlases overlaid to the template. Please note that some of the ATAG atlases have been estimated specifically to account for, e.g. age-related variance of the STN and are thus prone to vary from template anatomy (which is based on young subjects). *Also note that the Chakravarty 2006 histological atlas has been co-registered to the Colin 27 Average Brain template (Holmes et al. 1998) but is overlaid to a different template here. Even though both templates represent similar versions of the MNI space, inaccuracies on subcortical structures are prone to happen. STN definition from the Talairach Demon as defined by WFU Pickatlas (Lancaster et al. 2000; Maldjian et al. 2003). The version of the MIDA model was nonlinearly co-registered to standard space using a multimodal SyN deformation with Advanced Normalization Tools (Avants et al. 2008) as implemented in Lead-DBS. Selected axial slice cuts through two of three functional zones of the atlas by Accolla and colleagues (motor: red, associative: cyan). Bottom right panel shows all atlases overlaid to visualize their distribution. Axial sections displayed at z = -8 mm.

Methods

Data acquisition

The *2009a* and *b nonlinear* versions of the *MNI 152* template were obtained from the Montreal Neurological Institute at McGill University (http://www.bic.mni.mcgill.ca/ServicesAtlases/ICBM152NLin2009). The algorithm constructed in this study simultaneously worked on image acquisitions of different modalities. T1- and T2-weighted as well as proton density (PD) versions

of the high-resolution ICBM 152 2009b asymmetric template and T2 relaxometry (T2rlx) series of the 2009a symmetric template were used. A number of 20 point fiducials were marked on the STN and red nucleus (RN) using 3DSlicer software (http://www.slicer.org) within MNI space. 35 points were mapped for the pallidum.

Subcortical segmentation algorithm

The algorithm may be divided into three parts which are referenced as *first, second* and *third level* in the following. The goal of the first level was to maximize the number of tissue samples based on a low number of fiducial points *P* within the structure that were defined manually (see above). The intensity distribution of all fiducial points was sampled from each imaging modality. These values were averaged across fiducial points to form a reference intensity distribution *W* and the Euclidean distance *D* to the corresponding data vectors of each neighboring point of the starting fiducial points was calculated. Before calculating *D*, intensity values in each modality were z-scored so that distances in each modality had the same impact on *D*. The similarity *S* of each neighboring data point was calculated as follows:

$$S = \frac{1}{e^{f*D}}$$

where *f* is a penalty factor that determines the harshness of the relationship between *S* and *D*. On the first level, the goal was to find as many data samples of the anatomical structure as possible. However, it would have been fatal for consecutive steps to have the region grow outside the anatomical structure.

Therefore, a conservative value of f=0.05 was empirically chosen on the first level.

Values of S for each point were assigned to each neighboring datapoint whereas the initial points received a score of 1. In the first run, all points that received a score higher than 0.9 were added to the set of data points P. This threshold was updated to amount to the mean minus one standard deviation of all points in P until one thousand points were assigned. From then on, the threshold was held at this fixed value. The procedure was repeated fifty times or until no additional above-threshold point could be identified. From the second iteration on, W was calculated by using the mean across data points P weighted by their scores S.

The second level of the algorithm worked similarly but was not based on a region growing approach like the first level. Instead, the Mahalanobis distance between intensity profiles of each voxel in the brain and the intensity covariance structure defined on the final first level point set P was calculated. Here, only entries of P that had received a score S above the mean plus two standard deviations of all scores were taken into account. Mahalanobis distances obtained in this way were again transferred to score values based on **Equation 1**; however, to include more voxels into the resulting probabilistic map, a more liberal penalty factor of f=0.01 was chosen.

In this part of the algorithm, a predictive value V was calculated for each anatomical structure and each MRI modality. This value consisted of two components. First, the ratio between standard-deviation and mean value of intensities within P was calculated for each MR modality (V_1). The intuition of this value estimated how consistent the within-structure intensities of a certain

acquisition were. For instance, if the values of pallidal points in a T2-weighted image have a low standard deviation (relative to their mean value), the within-pallidal intensities are comparably consistent. The second part, V_2, instead focused on the specificity of a certain value in comparison to the rest of the brain. To assess this, the Mahalanobis distance between the mean intensity of *P* within a structure and all other points of the brain was calculated. This score is important because it gives insight into how *rare* a certain intensity range is for a given modality, i.e. how high the classification accuracy is for a certain structure. *V* was computed by multiplying V_1 and V_2. *V*, V_1 and V_2 were normalized to add up to a sum of 1 across acquisitions (**Table 1**).

Finally, on the third level of the algorithms, second level results for pallidum, red nucleus and STN were used to classify each voxel in a winner-takes-all fashion. Each voxel that received a score *S* above 0.3 in any of the three second level maps was assigned to the structure with the highest *S* across maps. The two largest components of this mapping were exported as a final binary mapping of STN, pallidum and red nucleus in both hemispheres.

The algorithm parameters were not modified for use in the exemplary single subject. However, images were upsampled to an isotropic space of 0.22 mm voxel size and lightly smoothed by using an isotropic Gaussian kernel with full-width half-maximum of 1 mm.

Manual labelling of target structures

Given the importance of a subsegmentation of the pallidum in deep brain stimulation (the internal part serves as a target in DBS whereas the external part is associated with side effects), the second level probability map of the pallidum

was used to further segment the pallidum into two parts manually (**Figure 4**). In the same process, STN and RN were again re-segmented manually. These manual segmentations of structures were performed on high definition (0.22 mm isotropic voxel size) versions of the template that had been generated using 7th degree Whittaker-Shannon (sinc) interpolation as implemented in SPM12. Here, *second level* results of the automated atlas version were used as primary guidance. Atlas structures were first defined on axial slices of the template using 3DSlicer software (www.slicer.org). For each nucleus surrounding structures were identified and the correct position of the segmented mask was verified and if necessary corrected on coronal and sagittal slices. Since STN is best visualized on T2-weighted acquisitions as reported by several groups (Kitajima et al. 2008; Slavin et al. 2006; Dormont et al. 2004), the T2-weighted version of the ICBM 2009b nonlinear template was chosen as secondary guidance for targets STN and RN. In addition to the *second level* maps, an anatomical delineation protocol was largely adopted and modified from (Pelzer et al. 2013). Explicitly, borders of the biconvex lens-shaped STN were largely identified by localizing surrounding structures on the coronal plane beginning with the red nucleus being a prominent structure on the T2-weighted template which was located medio-ventrally and in posterior direction from the STN. After location of the STN, its borders were defined by the substantia nigra located ventrally and slightly posterior. The posterior limb of the internal capsule located between GPi and STN was marked as the lateral border of the STN. The zone incerta marked the dorsal and slightly lateral borders; the fields of Forel H1 and H2 the dorsomedial ones. These structures appeared hyperintense on the T2-weighted template. In case of the internal and external pallidum the T1-weighted version of the template was used as secondary guidance in addition to *second level* maps. This decision was

informed by results in predictive values *V* that ranked highest in the T1-weighted template for the pallidum (see above and results section). The GPe was separated from the GPi by the internal or medial medullary lamina, whereas the external or lateral medullary lamina marked the lateral border of the GPe to the putamen. On T1, both laminae appeared significantly more hyperintense than the pallidum. On the coronal plane, the anterior limb of the internal capsule marked the anterior-medial borders of the pallidum. Further posterior, they were partly marked by the lenticular fascicles and by the genu and posterior limb of the internal capsule. Ventrally the pallidum was limited by the nucleus basalis Meynert as well as partly by the ventral pallidum and the anterior commissure. Anatomical borders were in close accordance to detailed neuroanatomical atlases (Augustine 2008; Mai et al. 2007). All structures, especially GPe and GPi, were defined on individual labels without informing the process by formerly labeled other structures. Only after completing the segmentation process all four structures were projected onto the same template to assess their position relatively to each other. Due to the close spatial relationship of GPe and GPi, this functioned as an additional control to assess whether their borders toward the internal medullary lamina were correctly positioned. The exact definition of these borders is crucial to localize placement of DBS-electrodes in the pallidum. Slight mistakes of <1mm would be revealed by either an overlap between the labels of GPe and GPi or by too wide a gap between their inner borders.

Results

Numbers of voxels included in the region growing algorithm (*first level*) are denoted as *Nvox* in **Table 1**, whereas mean intensity values used as *P* on the

second level are denoted as *I*. These values formed the distribution which Mahalanobis distances from each voxel were computed to. Additionally, consistency and specificity values ($V_{1/2}$) as well as overall predictive values (V) were computed for each target and sequence. The MR sequences with the best overall score to discriminate the STN were T2 followed by PD. The same order applied to the RN, whereas for the Pallidum, as expected, T1 followed by PD yielded highest scores.

The algorithm robustly segmented all three targets based on the multimodal ICBM 2009b template (*second level* results in **Figure 3** and **Figure 4**; *third level* results see **Figure 6** and **Figure 7**). Already on second level, the algorithm robustly shaped out all three structures (see **Figure 3** and **Figure 4**). In comparison to any of the single imaging modalities, second level maps yielded a high signal-to-noise contrast level that was helpful in the final manual segmentation process (**Figure 5**). Intensity values of pallidal subparts (GPe, GPi) were not found substantially different on either T1, T2, PD or T2rlx versions of the template by manual inspection. Thus, an automated segmentation between the subparts of the pallidum was not feasible.

Manual segmentations of all four structures (STN, RN, GPi, GPe) was performed on a high definition (0.22 mm isotropic voxel size) version of the template using *second level* results of the automated version of the atlas as primary guidance. In total, 63, 43, 48 and 36 axial slices were manually labeled for GPe, GPi, RN and STN respectively. Boundaries of resulting labels were subsequently corrected in coronal and sagittal views. In some border areas of the target structures, the high signal-to-noise contrast of *second level* maps constituted a helpful resource in the manual labeling process. As pointed out by Jovicich and colleagues, the

accurate and reliable measurement of subcortical brain volumes from MRI data is a non-trivial task (Jovicich et al. 2009). Moreover, due to the high resolution of the final output, the process amounted to ~90 hours of concentrated manual labeling. Despite this substantial effort, a high resolution of template space was chosen to attain high final resolution and to attain more robustness due to a more redundant re-labeling on each of two adjacent slices. Final results of both automated and manual versions of the atlas are visualized in **Figure 6** and **Figure 7**.

Final *third level* automated results estimated more conservative (i.e. smaller) results in comparison to manual labeling results. Volumes of manual segmentation amounted to 908 mm^3 (GPe), 369 mm^3 (GPi), 305 mm^3 (RN) and 130 mm^3 (STN). Volumes of the automated segmentation algorithm 1350 mm^3 (combined pallidum), 186 mm^3 (RN) and 86 mm^3 (STN). These differences in volumes again highlight the rather conservative approach of the third level winner-takes-all approach of the automated process (also see **Figure 7**). However, centroids of both parcellations were very similar: automated (x = ±10.96 mm, y = -12.26, z = -7.95) vs. manual STN (x = ±11.18 mm, y = -12.53 mm, z = -7.81 mm); automated (x = ±5.15 mm, y = -19.02 mm, z = -8.89 mm) vs. manual RN (x = ±5.18 mm, y = -19.06 mm, z = -8.96 mm). Centroid coordinates of automated GP were x = ±19.26 mm, y = -1.73 mm, z = -1.33 mm, whereas x = ±17.74 mm, y = -4.43 mm, z = -4.02 mm (GPi) and x = ±18.96 mm, y = -0.64 mm, z = -0.33 mm (GPe) were centroid coordinates of pallidal subparts in the manually segmented version.

Table 1: Behaviour of different MRI modalities in respect to the classification algorithm. Nvox denotes the number of voxels included in the first level (isotropic voxel size of 0.22 mm). These voxels served to form a distribution of multimodal intensities which constituted a reference for the Mahalanobis distance of each voxel on the second level. Consistency (V1), specificity (V2) and overall predictive value (V) are given for each MR sequence and each structure.

Modality	**T1**	**T2**	**PD**	**T2rlx**
STN	*(711 1st level voxels included)*			
Mean intensities (I)	70.36 ±0.33	39.01 ±0.44	56.90 ±0.34	0.08 ±0.00
Consistency (V1)	0.15	0.38	0.20	0.28
Specificity (V2)	0.06	0.49	0.40	0.05
Overall predictive value (V)	0.04	0.64	0.28	0.05
Pallidum	*(4699 1st level voxels included)*			
Mean intensities (I)	68.12 ±0.53	40.62 ±0.42	61.58 ±0.48	0.08 ±0.00
Consistency (V1)	0.33	0.25	0.25	0.17
Specificity (V2)	0.05	0.65	0.21	0.09
Overall predictive value (V)	0.73	0.05	0.18	0.05
RN	*(1203 st level voxels included)*			
Mean intensities (I)	68.45 ±0.22	42.80 ±0.41	58.82 ±0.24	0.09 ±0.00
Consistency (V1)	0.12	0.36	0.37	0.16
Specificity (V2)	0.06	0.49	0.40	0.06
Overall predictive value (V)	0.03	0.66	0.08	0.24

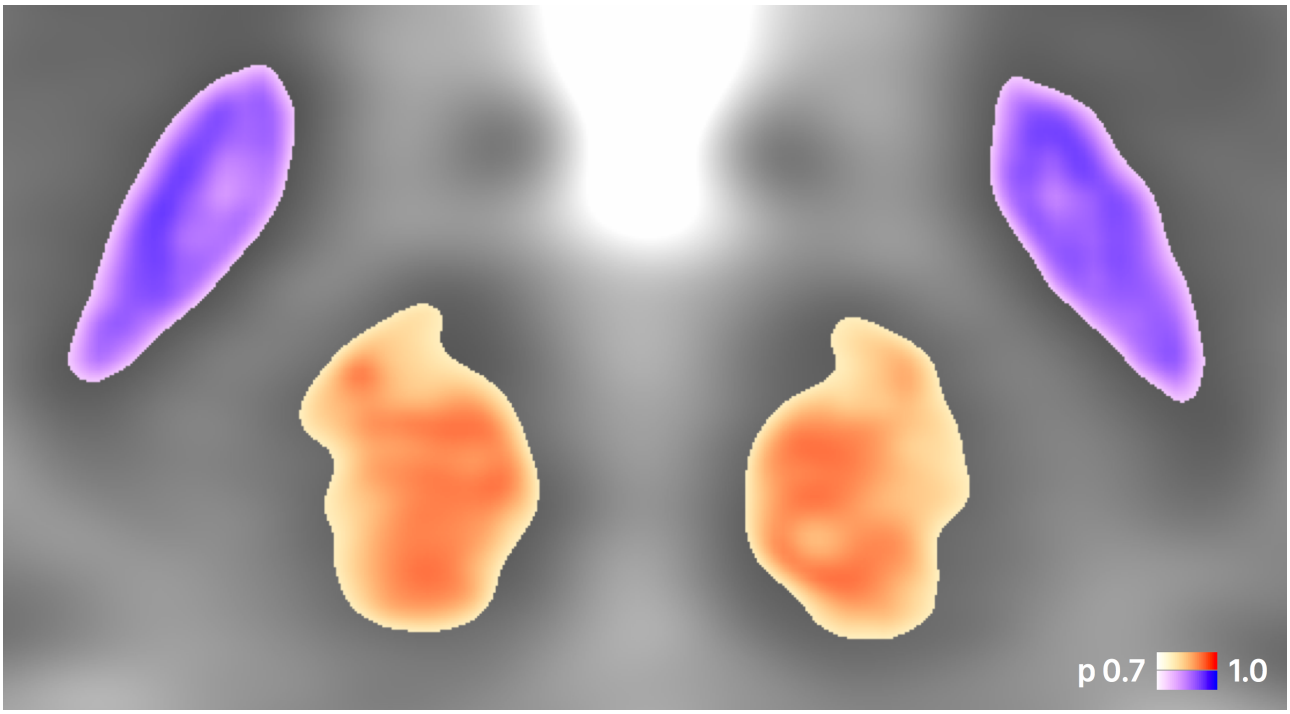

Figure 3: Multimodal probability maps for STN (cold tint) and RN (warm tint) as estimated using the ICBM 152 template. Results of the second level are shown. Based on manually defined fiducial points that served as starting coordinates for a region growing algorithm in each structure, a large number of tissue sample points of the STN and RN could be generated automatically. These served as a multimodal probability distribution which Mahalanobis distance was calculated to for each voxel in the brain.

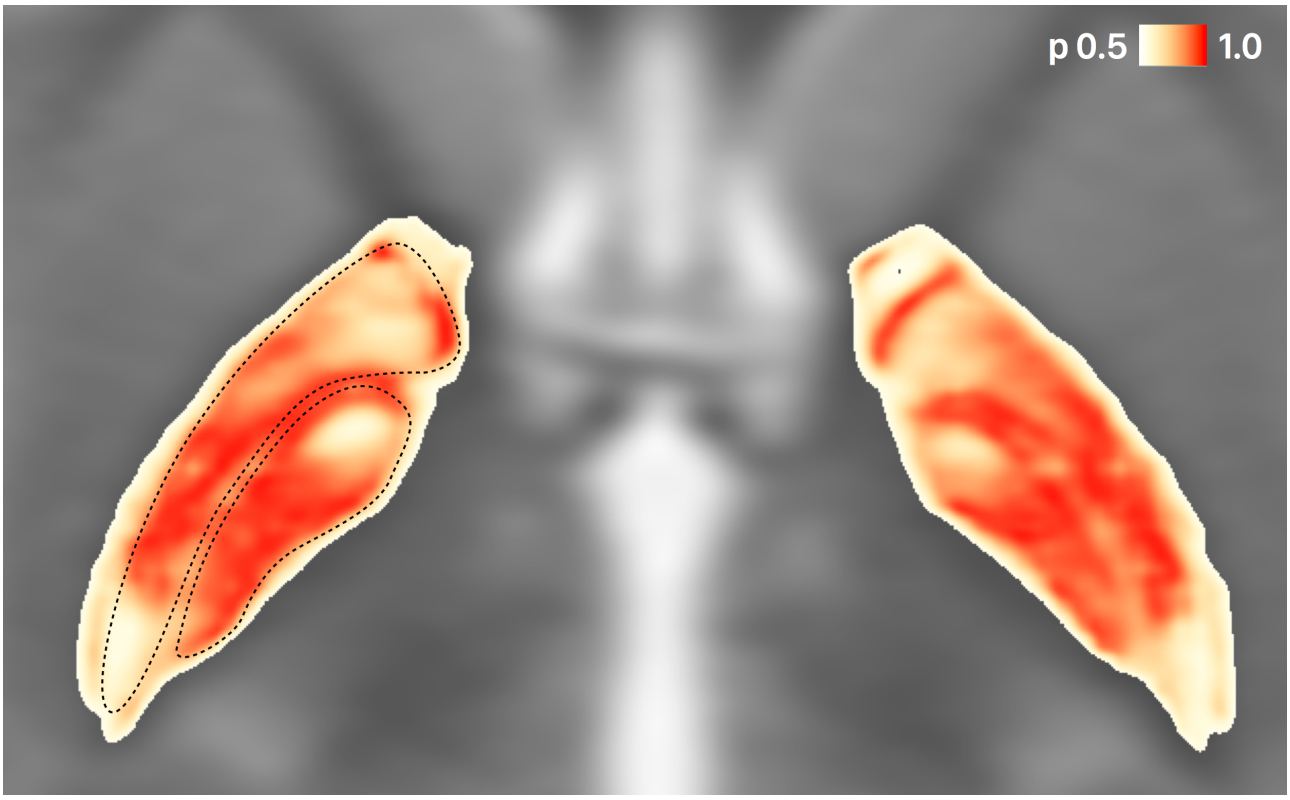

Figure 4: Multimodal probability map of the pallidum as estimated using the ICBM 152 template. Results of the second level are shown. Please note that the external and internal parts of the pallidum can be clearly outlined based on this computation by visual inspection. An automated segmentation between the subparts of the pallidum was not feasible given their very similar intensity distribution across acquisitions. However, based on the computational results, the two structures were segmented manually (dashed lines, shown for the right hemisphere as an example) for the final atlas. Axial slice at z = -2.6 mm.

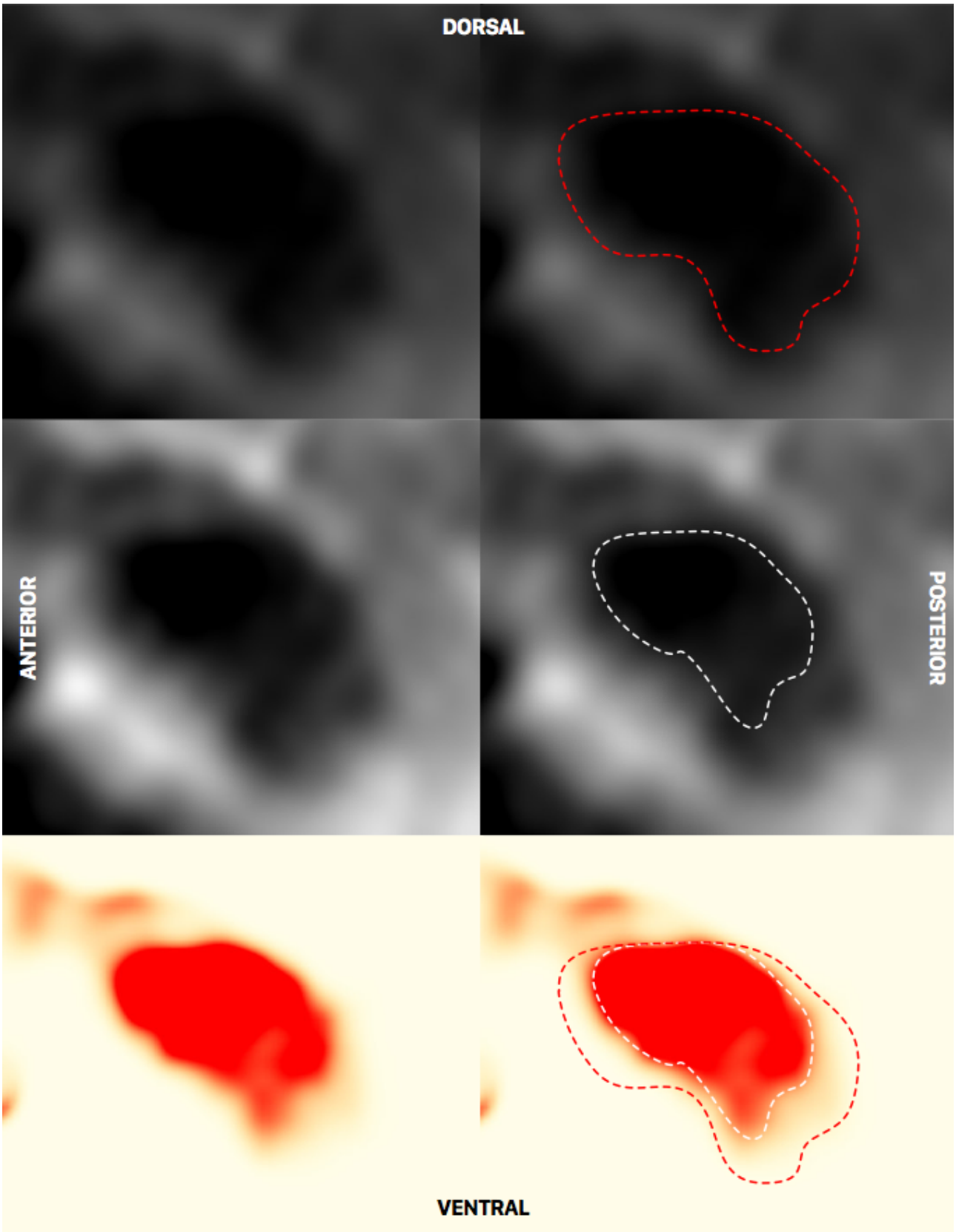

Figure 5: Sagittal slice of the T2-weighted ICBM template at x = -7.3 mm. Here, depending on windowing, the RN appears substantially larger (top) or smaller

(middle). The RN second-level probability map (bottom) exhibits a much higher signal-to-noise ratio and is helpful in determining the ventral anatomical border of the nucleus in the process of manual segmentation. Based on neighboring slices, the correctness of the map could be confirmed to result from a partial volume effect.

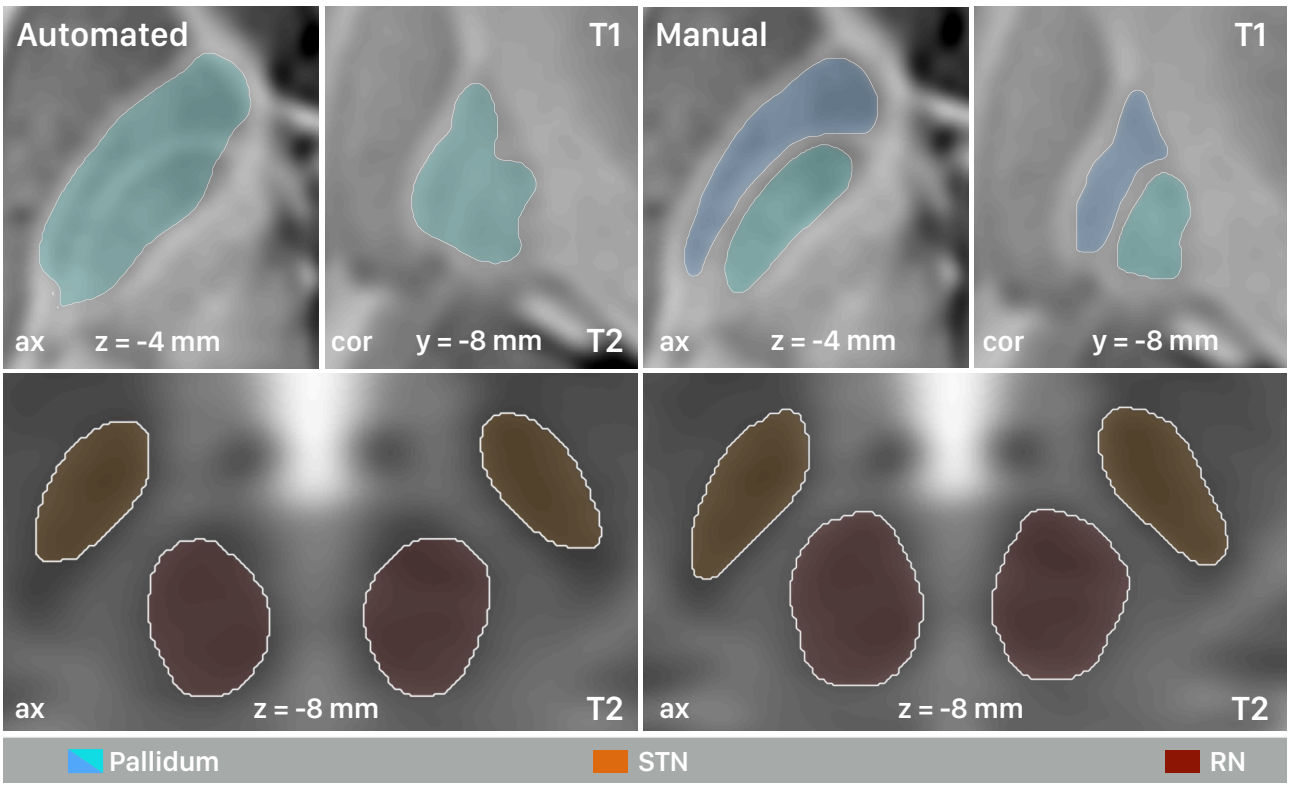

Figure 6: Final fully automated (third-level) parcellation of the template (left half). No manual thresholding or further post processing was performed. In comparison to the second level, on this final level of the processing stream, a binary classification is obtained. Final manual parcellation of the template (right half). Structures were defined in a 0.22 mm isotropic resolution.

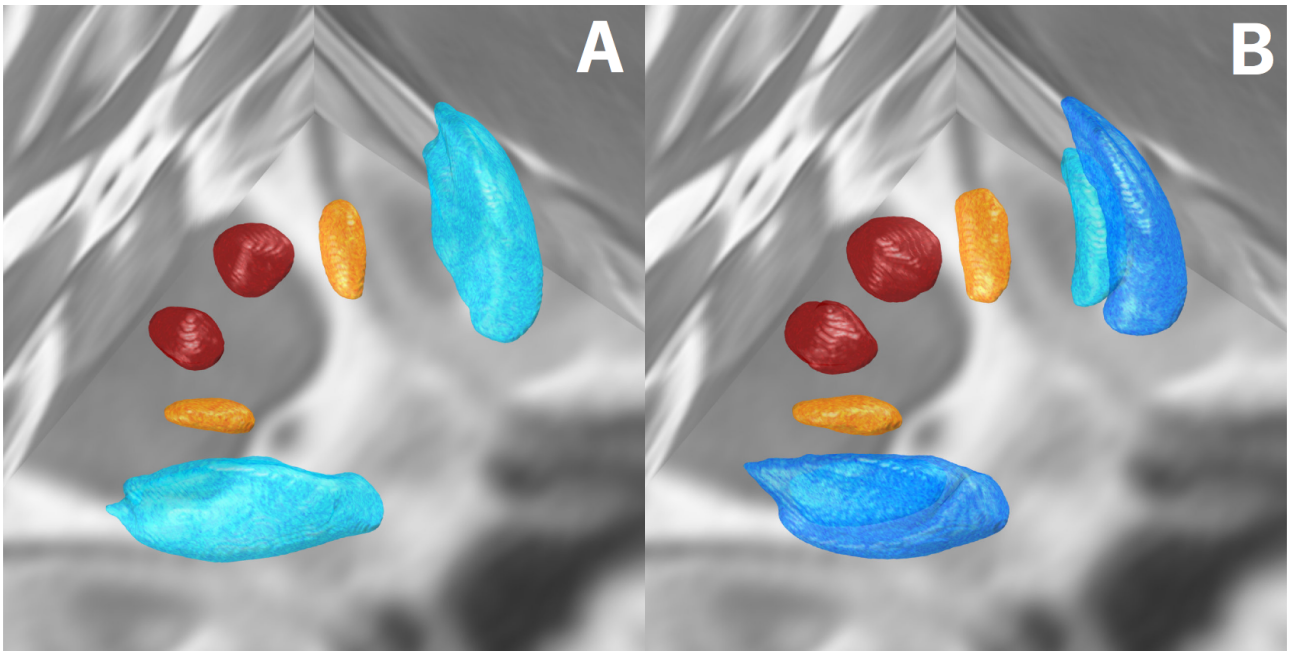

Figure 7: Final automated (A) and manually segmented (B) atlases based on the ICBM 152 2009 template series. The left version of the atlas has been generated in a fully automated and observer independent fashion but does not differentiate between internal and external parts of the pallidum. The right version has been segmented manually but was informed by the automated probability maps to maximize objectivity. Note that the automated version resulted in smaller parcellations due to reasons of robustness of the algorithm. Both versions are being made publicly available under an open license.

Discussion

Results of this study show that it is possible to robustly segment subcortical structures from a high-resolution MNI template based on a low number of manually placed fiducial points residing within each subcortical structure. In particular, the algorithm was employed on three modalities of the ICBM 2009b and one of the 2009a nonlinear standard brain templates to estimate a subcortical atlas that exactly matched the anatomy of structures as defined by

the templates in shape, size and position. The two primary targets for deep brain stimulation, the STN and the pallidum, as well as the red nucleus were extracted from the template, given the great clinical interest in these structures. The latter was additionally selected because a high robustness of the spatial relationship between RN and STN has been described in the past and because the RN is conventionally used as a waypoint in surgical planning for STN-DBS ((Andrade-Souza et al. 2008; Starr et al. 2002; Pollo et al. 2003) but also see (Danish et al. 2006)).

Despite the simplicity of the proposed algorithm, it is completely independent from the MR acquisitions used. In other words, it is not dependent on a fixed set of e.g. T2, T1 and PD sequences. Rather, the more acquisitions present for a certain dataset, the more robust the results would be. The algorithm could potentially be applied to multimodal single subject datasets in the future. However, the focus of this study was not to create a subcortical segmentation algorithm. Potentially superior algorithms that automatically segment subcortical structures in the brain already exist as open source (e.g. see (Patenaude et al. 2011); http://fsl.fmrib.ox.ac.uk/fsl/fslwiki/FIRST; or (Wang et al. 2014); https://www.nitrc.org/projects/autoseg/). Despite the fact that these algorithms do not focus on DBS targets (e.g. the STN is not implemented in out-of-the-box versions of FIRST or AutoSeg), they could potentially be extended to support these. Alternatively, tools for robust manual segmentations are also available (e.g. see (Haegelen et al. 2013); http://www.itksnap.org/) and recently, novel tissue probability maps that include all important subcortical structures and may be used within the popular segmentation algorithm of SPM have been established (Lorio et al. 2016).

Instead, the main focus of this study was to generate an atlas that defined the exact spatial location and extent of the two most commonly used DBS targets in standard stereotactic MNI/ICBM 152 2009 nonlinear space. As mentioned in the introduction, several subcortical atlases exist that stem from various sources (Prodoehl et al. 2008; Keuken et al. 2013; Qiu et al. 2010; Jakab et al. 2012; Chakravarty et al. 2006; Yelnik et al. 2007; Krauth et al. 2010; Keuken et al. 2014; Morel 2013). The anatomical detail of some of the available atlases goes far beyond the data presented here. Still, we argue that a proper spatial definition of DBS targets *within* the standard brain template adopted by the ICBM may be a crucial prerequisite for group studies that analyze the relationship between spatial locations of DBS electrodes with respect to anatomical targets and clinical outcomes. In comparison to single subject analyses, these studies depend on spatial normalization into a common space and a proper and observer-independent definition of the anatomical target herein. Before, studies with similar goals have overcome the issue by nonlinearly coregistering patient data to the space of a certain atlas (instead of the ICBM template; e.g. (Yelnik et al. 2007; Welter et al. 2014; Butson et al. 2007)) or by segmenting the STN into geometrical subfields within each patient's native space (Herzog et al. 2004; Wodarg et al. 2012). A disadvantage of these approaches may be that they do not use the full potential of years in research that have gone both into developing standardized, study-independent and well-characterized anatomical templates (Fonov et al. 2011b; Fonov et al. 2009; Allen et al. 2002) and into the steadily ongoing evolution of nonlinear deformation algorithms (Ashburner 2007; Ashburner 2012; Avants et al. 2011; Avants et al. 2008; Klein et al. 2009). Even more importantly, results are not generalizable to novel patient populations if the atlases and/or atlas templates are not broadly available. Another potential

application of our atlas could be to assist in the process of warping more detailed atlases into standard space. Especially datasets defined on histological stacks (Morel 2013; Chakravarty et al. 2006; Yelnik et al. 2007) could be co-registered into MNI space using additional spatial information of our atlas as anchor points. Histological atlases give detailed insight into surrounding structures of DBS targets that have played a prominent role in DBS targeting research, such as the zona incerta (Karlsson et al. 2011; Schmitz-Hubsch et al. 2014; Plaha et al. 2006; Blomstedt et al. 2012) or the dentatorubrothalamic tract (Meola et al. 2015; Coenen et al. 2011). But if their definition of the main targets does not exactly match the ones of the template used for nonlinear co-registration, the information gained from the use of such atlases may in certain cases be misleading.

Finally, as an important limitation to our atlas, we would like to raise a different question. In the caption of **Figure 1**, we asked *which* atlas was correct. However, for many applications, this is the wrong question to ask altogether. Instead, «*what* is correct?» should be asked. A good example is the ATAG dataset of STN atlases which exists for three age populations (Keuken et al. 2013). In our view, both its publication and release to the community under an open license were extraordinarily valuable contributions to the neuroscientific community since they clearly showed that position and shape of the STN varies with subject age and made the data available for everyone to examine directly. Thus, while our atlas set tries to maximize overlap with the ICBM template, the approach of Keuken and colleagues was the opposite: to uncover and define anatomical variability of the nucleus. We argue that both goals are valid and may help to answer the questions for which they were designed. A prerequisite of the

(absolute) validity of our approach is the (absolute) correctness of normalization results obtained from nonlinear deformation algorithms. Of course, despite the increasing accuracy of the latter, this prerequisite is not fulfilled in practice. Most nonlinear deformation algorithms even introduce penalty equations that prevent them from extreme overfitting and high inhomogeneity of deformation fields at some point. Another reason is that DBS targets may not exhibit a large enough contrast for the algorithm to create an accurate deformation – especially when using MRI data acquired in a clinical setting. Given these reasons, datasets like the one introduced by Keuken and colleagues may be of great value when studying a certain age population.

Other limitations include the aforementioned partial disagreement between the STN as visualized in MRI and in reality. The dorsolateral part of the nucleus (which corresponds to its sensorimotor functional zone) does not show as hypointense as the ventromedial part (Richter et al. 2004). This fact besides many other reasons justifies the use of histological atlases if they are correctly co-registered to a specific template of choice.

Conclusion

In this study, an observer-independent definition of two prominent deep brain stimulation targets within the ICBM 2009 152 template series was delineated. Additionally, a manually segmented atlas was defined in high resolution that was largely informed by automatically generated probability maps. The atlas data may be used for studies that analyze the relationship between deep brain stimulation electrodes and their anatomical targets within ICBM2009b asymmetric space in a volumetric fashion. The atlas data will be made publicly

available to the scientific community under an open license using the name DISTAL atlas (**D**BS **I**ntrin**s**ic **T**emplate **A**t**L**as). It will be distributed within the software package Lead-DBS (www.lead-dbs.org).

Acknowledgments

The study was supported by the German Research Agency (DFG - Deutsche Forschungsgemeinschaft). Grant Number: KFO 247.

SE and AH received funding from Stiftung Charité, Max-Rubner-Preis; AH further received funding from Berlin Institute of Health and Prof. Klaus Thiemann Foundation.

Bibliography

Allen, J.S., Damasio, H. & Grabowski, T.J., 2002. Normal neuroanatomical variation in the human brain: An MRI–volumetric study. *American Journal of Physical Anthropology*, 118(4), pp.341–358. Available at: http://doi.wiley.com/10.1002/ajpa.10092.

Andrade-Souza, Y.M. et al., 2008. Comparison of three methods of targeting the subthalamic nucleus for chronic stimulation in Parkinson's disease. *Neurosurgery*, 62 Suppl 2, pp.875–883. Available at: http://eutils.ncbi.nlm.nih.gov/entrez/eutils/elink.fcgi?dbfrom=pubmed&id=18596420&retmode=ref&cmd=prlinks.

Ashburner, J., 2007. A fast diffeomorphic image registration algorithm. , 38(1), pp.95–113. Available at: http://linkinghub.elsevier.com/retrieve/pii/S1053811907005848.

Ashburner, J., 2012. SPM: a history. Available at: http://www.sciencedirect.com/science/article/pii/S1053811911011888.

Augustine, J.R., 2008. Human Neuroanatomy. , p.494.

Avants, B.B. et al., 2011. A reproducible evaluation of ANTs similarity metric performance in brain image registration. *NeuroImage*, 54(3), pp.2033–2044. Available at: http://linkinghub.elsevier.com/retrieve/pii/S1053811910012061.

Avants, B.B. et al., 2008. Symmetric diffeomorphic image registration with cross-correlation: evaluating automated labeling of elderly and neurodegenerative brain. *Medical image analysis*, 12(1), pp.26–41. Available at: http://linkinghub.elsevier.com/retrieve/pii/S1361841507000606.

Barow, E. et al., 2014. Deep brain stimulation suppresses pallidal low frequency activity in patients with phasic dystonic movements. *Brain : a journal of neurology*, 137, pp.3012–3024. Available at: http://www.brain.oxfordjournals.org/cgi/doi/10.1093/brain/awu258.

Blomstedt, P. et al., 2012. Unilateral caudal zona incerta deep brain stimulation for Parkinsonian tremor. *Parkinsonism & related disorders*, 18(10), pp.1062–1066. Available at: http://dx.doi.org/10.1016/j.parkreldis.2012.05.024.

Brett, M., Johnsrude, I.S. & Owen, A.M., 2002. The problem of functional localization in the human brain. *Nature Reviews Neuroscience*, 3(3), pp.243–249. Available at: http://www.nature.com/doifinder/10.1038/nrn756.

Butson, C.R. et al., 2007. Patient-specific analysis of the volume of tissue activated during deep brain stimulation. , 34(2), pp.661–670. Available at: http://linkinghub.elsevier.com/retrieve/pii/S1053811906009669.

Chakravarty, M.M. et al., 2006. The creation of a brain atlas for image guided neurosurgery using serial histological data. *NeuroImage*, 30(2), pp.359–376. Available at: http://linkinghub.elsevier.com/retrieve/pii/S1053811905006993.

Coenen, V.A., Allert, N. & Mädler, B., 2011. A role of diffusion tensor imaging fiber tracking in deep brain stimulation surgery: DBS of the dentato-rubro-thalamic tract (drt) for the treatment of therapy-refractory tremor. *Acta neurochirurgica*, 153(8), p.1579. Available at: http://eutils.ncbi.nlm.nih.gov/entrez/eutils/elink.fcgi?dbfrom=pubmed&id=21553318&retmode=ref&cmd=prlinks.

Collins, D.L., 1994. 3D Model-based Segmentation of Individual Brain Structures from Magnetic Resonance Imaging Data. , p.478. Available at: http://www.bic.mni.mcgill.ca/users/louis/papers/phd_thesis/collinsphd94.ps.gz.

Danish, S.F. et al., 2006. Conventional MRI is inadequate to delineate the relationship between the red nucleus and subthalamic nucleus in Parkinson's disease. *Stereotactic and functional neurosurgery*, 84(1), pp.12–18. Available at: http://www.karger.com/doi/10.1159/000092682.

Diedrichsen, J. et al., 2011. Imaging the deep cerebellar nuclei: a probabilistic atlas and normalization procedure. *NeuroImage*, 54(3), pp.1786–1794. Available at: http://linkinghub.elsevier.com/retrieve/pii/S1053811910013273.

Dormont, D., Ricciardi, K.G. & Tandé, D., 2004. Is the subthalamic nucleus hypointense on T2-weighted images? A correlation study using MR imaging and stereotactic atlas data. *AJNR American journal of neuroradiology*. Available at: http://www.ajnr.org/content/25/9/1516.short.

Eisenstein, S.A. et al., 2014. Functional anatomy of subthalamic nucleus stimulation in Parkinson disease. *Annals of neurology*, 76(2), pp.279–295. Available at: http://onlinelibrary.wiley.com/doi/10.1002/ana.24204/full.

Fonov, V. et al., 2011a. Unbiased average age-appropriate atlases for pediatric studies. *NeuroImage*, 54(1), pp.313–327. Available at: http://linkinghub.elsevier.com/retrieve/pii/S1053811910010062.

Fonov, V. et al., 2011b. Unbiased average age-appropriate atlases for pediatric studies. , 54(1), pp.313–327. Available at: http://linkinghub.elsevier.com/retrieve/pii/S1053811910010062.

Fonov, V.S. et al., 2009. Unbiased nonlinear average age-appropriate brain templates from birth to adulthood. *NeuroImage*, 47, p.S102. Available at: http://linkinghub.elsevier.com/retrieve/pii/S1053811909708845.

Frankemolle, A.M.M. et al., 2010. Reversing cognitive-motor impairments in Parkinson's disease patients using a computational modelling approach to deep brain stimulation programming. *Brain : a journal of neurology*, 133, pp. 746–761. Available at: http://www.brain.oxfordjournals.org/cgi/doi/10.1093/brain/awp315.

Haegelen, C. et al., 2013. Automated segmentation of basal ganglia and deep brain structures in MRI of Parkinson's disease. *International Journal of Computer Assisted Radiology and Surgery*, 8(1), pp.99–110. Available at: http://link.springer.com/10.1007/s11548-012-0675-8.

Herzog, J. et al., 2004. Most effective stimulation site in subthalamic deep brain stimulation for Parkinson's disease. *Movement disorders : official journal of*

the Movement Disorder Society, 19(9), pp.1050–1054. Available at: http://doi.wiley.com/10.1002/mds.20056.

De Hollander, G. et al., 2014. A gradual increase of iron toward the medial-inferior tip of the subthalamic nucleus. *Human Brain Mapping*, 35(9), pp.4440–4449. Available at: http://doi.wiley.com/10.1002/hbm.22485.

Horn, A. & Kühn, A.A., 2015a. Lead-DBS: a toolbox for deep brain stimulation electrode localizations and visualizations. *NeuroImage*, 107, pp.127–135. Available at: http://eutils.ncbi.nlm.nih.gov/entrez/eutils/elink.fcgi?dbfrom=pubmed&id=25498389&retmode=ref&cmd=prlinks.

Horn, A. & Kühn, A.A., 2015b. Lead-DBS: a toolbox for deep brain stimulation electrode localizations and visualizations. *NeuroImage*, 107, pp.127–135. Available at: http://eutils.ncbi.nlm.nih.gov/entrez/eutils/elink.fcgi?dbfrom=pubmed&id=25498389&retmode=ref&cmd=prlinks.

Iacono, M.I. et al., 2015. MIDA: A Multimodal Imaging-Based Detailed Anatomical Model of the Human Head and Neck. *PLoS ONE*, 10(4), p.e0124126. Available at: http://dx.plos.org/10.1371/journal.pone.0124126.

Jakab, A. et al., 2012. Generation of Individualized Thalamus Target Maps by Using Statistical Shape Models and Thalamocortical Tractography. *AJNR American journal of neuroradiology*, 33(11), pp.2110–2116. Available at: http://www.ajnr.org/content/33/11/2110.full.

Jovicich, J. et al., 2009. MRI-derived measurements of human subcortical, ventricular and intracranial brain volumes: Reliability effects of scan sessions, acquisition sequences, data analyses, scanner upgrade, scanner vendors and

field strengths. *NeuroImage*, 46(1), pp.177–192. Available at: http://linkinghub.elsevier.com/retrieve/pii/S1053811909001505.

Karlsson, F. et al., 2011. Deep Brain Stimulation of Caudal Zona Incerta and Subthalamic Nucleus in Patients with Parkinson's Disease: Effects on Diadochokinetic Rate. *Parkinson's Disease*, 2011(1), pp.1–10. Available at: http://www.hindawi.com/journals/pd/2011/605607/.

Keuken, M.C. et al., 2014. Quantifying inter-individual anatomical variability in the subcortex using 7T structural MRI. , 94, pp.40–46. Available at: http://linkinghub.elsevier.com/retrieve/pii/S1053811914001797.

Keuken, M.C. et al., 2013. Ultra-high 7T MRI of structural age-related changes of the subthalamic nucleus. , 33(11), pp.4896–4900. Available at: http://eutils.ncbi.nlm.nih.gov/entrez/eutils/elink.fcgi?dbfrom=pubmed&id=23486960&retmode=ref&cmd=prlinks.

Kitajima, M. et al., 2008. Human subthalamic nucleus: evaluation with high-resolution MR imaging at 3.0 T. *Neuroradiology*, 50(8), pp.675–681. Available at: http://link.springer.com/10.1007/s00234-008-0388-4.

Klein, A. et al., 2009. Evaluation of 14 nonlinear deformation algorithms applied to human brain MRI registration. , 46(3), pp.786–802. Available at: http://eutils.ncbi.nlm.nih.gov/entrez/eutils/elink.fcgi?dbfrom=pubmed&id=19195496&retmode=ref&cmd=prlinks.

Krauth, A. et al., 2010. A mean three-dimensional atlas of the human thalamus: Generation from multiple histological data. , 49(3), pp.2053–2062. Available at: http://linkinghub.elsevier.com/retrieve/pii/S1053811909011136.

Lenglet, C. et al., 2012. Comprehensive in vivo mapping of the human basal ganglia and thalamic connectome in individuals using 7T MRI. *PLoS ONE*, 7(1), p.e29153. Available at: http://eutils.ncbi.nlm.nih.gov/entrez/eutils/elink.fcgi?dbfrom=pubmed&id=22235267&retmode=ref&cmd=prlinks.

Liang, P. et al., 2015. Construction of brain atlases based on a multi-center MRI dataset of 2020 Chinese adults. *Scientific Reports*, 5, p.18216. Available at: http://www.nature.com/srep/2015/151218/srep18216/full/srep18216.html.

Lorio, S. et al., 2016. New tissue priors for improved automated classification of subcortical brain structures on MRI. *NeuroImage*, 130, pp.157–166. Available at: http://linkinghub.elsevier.com/retrieve/pii/S1053811916000926.

Mai, J.K., Paxinos, G. & Voss, T., 2007. Atlas of the Human Brain. , pp.1–279.

Meola, A. et al., 2015. The nondecussating pathway of the dentatorubrothalamic tract in humans: human connectome-based tractographic study and microdissection validation. *Journal of neurosurgery*, pp.1–7. Available at: http://thejns.org/doi/10.3171/2015.4.JNS142741.

Merkl, A. et al., 2014. Association Between Beta Oscillations in the Subcallosal Cortex and Emotion Processing in Depressed Patients. *Society of Biological Psychiatry th Annual Meeting*, p.1.

Merkl, A. et al., 2015. Modulation of Beta-Band Activity in the Subgenual Anterior Cingulate Cortex during Emotional Empathy in Treatment-Resistant Depression. *Cerebral cortex (New York, N.Y. : 1991)*. Available at: http://www.cercor.oxfordjournals.org/cgi/doi/10.1093/cercor/bhv100.

Morel, A., 2013. Stereotactic Atlas of the Human Thalamus and Basal Ganglia. , p. 160. Available at: http://books.google.de/books?id=b9m3dlu2kX4C&printsec=frontcover&dq=Stereotactic+Atlas+of+the+Human+Thalamus+and+Basal+Ganglia&hl=&cd=1&source=gbs_api.

Neumann, W.-J., Jha, A., et al., 2015. Cortico-pallidal oscillatory connectivity in patients with dystonia. *Brain : a journal of neurology*, 138, pp.1894–1906. Available at: http://www.brain.oxfordjournals.org/lookup/doi/10.1093/brain/awv109.

Neumann, W.-J., Staub, F., et al., 2015. Deep Brain Recordings Using an Implanted Pulse Generator in Parkinson's Disease. *Neuromodulation: Technology at the Neural Interface*. Available at: http://eutils.ncbi.nlm.nih.gov/entrez/eutils/elink.fcgi?dbfrom=pubmed&id=26387795&retmode=ref&cmd=prlinks.

Patenaude, B. et al., 2011. A Bayesian model of shape and appearance for subcortical brain segmentation. Available at: http://www.sciencedirect.com/science/article/pii/S1053811911002023.

Pelzer, E.A. et al., 2013. Cerebellar networks with basal ganglia: feasibility for tracking cerebello-pallidal and subthalamo-cerebellar projections in the human brain. *European Journal of Neuroscience*, 38(8), pp.3106–3114. Available at: http://doi.wiley.com/10.1111/ejn.12314.

Plaha, P. et al., 2006. Stimulation of the caudal zona incerta is superior to stimulation of the subthalamic nucleus in improving contralateral parkinsonism. , 129, pp.1732–1747. Available at: http://eutils.ncbi.nlm.nih.gov/

entrez/eutils/elink.fcgi?
dbfrom=pubmed&id=16720681&retmode=ref&cmd=prlinks.

Pollo, C. et al., 2004. Magnetic resonance artifact induced by the electrode Activa 3389: an in vitro and in vivo study. *Acta neurochirurgica*, 146(2), pp.161–164. Available at: http://link.springer.com/10.1007/s00701-003-0181-4.

Pollo, C. et al., 2003. Subthalamic nucleus deep brain stimulation for Parkinson's disease: magnetic resonance imaging targeting using visible anatomical landmarks. *Stereotactic and functional neurosurgery*, 80(1), pp.76–81. Available at: http://www.karger.com/Article/FullText/75163.

Prodoehl, J. et al., 2008. Region of interest template for the human basal ganglia: Comparing EPI and standardized space approaches. , 39(3), pp.956–965. Available at: http://linkinghub.elsevier.com/retrieve/pii/S1053811907008117.

Qiu, A. et al., 2010. Atlas generation for subcortical and ventricular structures with its applications in shape analysis. *IEEE transactions on image processing : a publication of the IEEE Signal Processing Society*, 19(6), pp.1539–1547. Available at: http://eutils.ncbi.nlm.nih.gov/entrez/eutils/elink.fcgi?dbfrom=pubmed&id=20129863&retmode=ref&cmd=prlinks.

Richter, E.O. et al., 2004. Determining the position and size of the subthalamic nucleus based on magnetic resonance imaging results in patients with advanced Parkinson disease. *Journal of neurosurgery*, 100(3), pp.541–546. Available at: http://eutils.ncbi.nlm.nih.gov/entrez/eutils/elink.fcgi?dbfrom=pubmed&id=15035292&retmode=ref&cmd=prlinks.

Schäfer, A. et al., 2011. Direct visualization of the subthalamic nucleus and its iron distri... - PubMed - NCBI. *Human Brain Mapping*, 33(12), pp.2831–2842. Available at: http://doi.wiley.com/10.1002/hbm.21404.

Schmitz-Hubsch, T. et al., 2014. The caudal zona incerta does not prove suitable as a target for deep brain stimulation in Parkinson's disease. *International Parkinson and Movement Disorder Society MDS*, pp.1–2.

Slavin, K.V., Thulborn, K.R. & Wess, C., 2006. Direct visualization of the human subthalamic nucleus with 3T MR imaging. *AJNR American journal of neuroradiology*. Available at: http://www.ajnr.org/content/27/1/80.short.

Starr, P.A. et al., 2002. Implantation of deep brain stimulators into subthalmic nucleus: technical approach and magnetic imaging—verified electrode locations. *Journal of neurosurgery*, 97(2), pp.370–387. Available at: http://thejns.org/doi/abs/10.3171/jns.2002.97.2.0370.

Wang, J. et al., 2014. Multi-atlas segmentation of subcortical brain structures via the AutoSeg software pipeline. *Frontiers in neuroinformatics*, 8, p.7. Available at: http://journal.frontiersin.org/article/10.3389/fninf.2014.00007/abstract.

Wang, Y. & Liu, T., 2015. Quantitative susceptibility mapping (QSM): Decoding MRI data for a tissue magnetic biomarker. *Magnetic Resonance in Medicine*, 73(1), pp.82–101. Available at: http://onlinelibrary.wiley.com/doi/10.1002/mrm.25358/full.

Welter, M.-L. et al., 2014. Optimal target localization for subthalamic stimulation in patients with Parkinson disease. *Neurology*, 82(15), pp.1352–1361. Available at: http://www.neurology.org/cgi/doi/10.1212/WNL.0000000000000315.

Wodarg, F. et al., 2012. Stimulation site within the MRI-defined STN predicts postoperative motor outcome. *Movement disorders : official journal of the Movement Disorder Society*, 27(7), pp.874–879. Available at: http://doi.wiley.com/10.1002/mds.25006.

Yelnik, J. et al., 2007. A three-dimensional, histological and deformable atlas of the human basal ganglia. I. Atlas construction based on immunohistochemical and MRI data. , 34(2), pp.618–638. Available at: http://linkinghub.elsevier.com/retrieve/pii/S1053811906009700.

Yelnik, J. et al., 2003. Localization of stimulating electrodes in patients with Parkinson disease by using a three-dimensional atlas-magnetic resonance imaging coregistration method. *Journal of neurosurgery*, 99(1), pp.89–99. Available at: http://thejns.org/doi/abs/10.3171/jns.2003.99.1.0089.